J. Fluid Mech. (1990), *vol.* 211, *pp.* 529–556
Printed in Great Britain

Turbulent boundary layer relaxation from convex curvature

By AMY E. ALVING,† ALEXANDER J. SMITS AND JONATHAN H. WATMUFF‡
Department of Mechanical and Aerospace Engineering, Princeton University, Princeton, NJ 08544, USA

(Received 10 February 1989 and in revised form 13 July 1989)

A study was undertaken to examine the flat plate relaxation behaviour of a turbulent boundary layer recovering from 90° of strong convex curvature ($\delta_0/R = 0.08$), for a length of $\approx 90\delta_0$ after the end of curvature, where δ_0 is the boundary layer thickness at the start of the curvature. The results show that the relaxation behaviour of the mean flow and the turbulence are quite different. The mean velocity profile and skin friction coefficient asymptotically approach the unperturbed state and at the last measuring station appear to be fully recovered. The turbulence relaxation, however, occurs in several stages over a much longer distance. In the first stage, a stress 'bore' (a region of elevated stress) is generated near the wall, and the bore thickens with distance downstream. Eventually it fills the whole boundary layer, but the stress levels continue to rise beyond their self-preserving values. Finally the stresses begin a gradual decline, but at the last measuring station they are still well above the unperturbed levels, and the ratios of the Reynolds stresses are distorted. These results imply a reorganization of the large-scale structure into a new quasi-stable state. The long-lasting effects of curvature highlight the sensitivity of a boundary layer to its condition of formation.

1. Introduction

In this paper, we describe an experimental study of the relaxation behaviour of a turbulent boundary layer perturbed by a region of strong convex curvature. The behaviour of a boundary layer downstream of a strong perturbation provides useful information concerning the effect of upstream history on the downstream flow. Recently, there has also been interest in the use of curvature as a means of drag reduction because convex curvature reduces skin friction (Bushnell 1983). The relaxation behaviour is therefore important from a practical viewpoint, as it determines how far downstream the drag reduction can be expected to continue.

The response to the *application* of strong convex curvature, $\delta_0/R \geqslant 0.05$, is now reasonably well known, mainly through the experiments by So & Mellor (1973) ($0.05 < \delta_0/R < 0.07$), Gillis *et al.* (1980) and Gillis & Johnston (1983) (three similar studies, $\delta_0/R = 0.05$ and 0.1). In all cases, convex curvature strongly reduced the

† Present address: Herman-Fottinger Institute, Technical University of Berlin, D-1000 Berlin 12, FGR.
‡ Present address: Center for Turbulence Research, NASA-Ames Research Center MS 260-1, Moffett Field, CA 94035, USA.

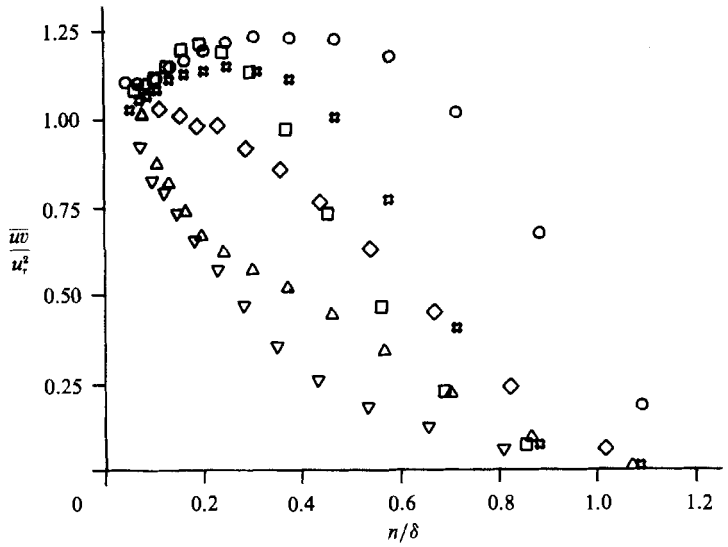

FIGURE 1. Reynolds shear stress, from Gillis *et al.* (1980): ◇, upstream reference; △, 13° convex curvature; ▽, 52° convex curvature; □, $s/\delta_0 = 7.9$; ⊠, $s/\delta_0 = 21$; ○, $s/\delta_0 = 42$ (s is measured from the end of the curved section).

turbulent mixing, resulting in a low skin friction and in mean velocity profiles which lacked fullness. The Reynolds stress levels were also strongly reduced, as shown for the shear stress in figure 1. As expected, this effect was more pronounced in the outer half of the boundary layer, where the ratio of the 'extra' strain rate due to curvature $\partial V/\partial x$ divided by the principal strain rate $\partial U/\partial y$ was largest (Bradshaw 1973). There the shear was 'turned off' (So & Mellor) and the normal stresses approached isotropy. Gillis & Johnston found that after 30° of turning, their shear stress profiles and those of So & Mellor collapsed when the distance from the wall, y, was scaled on R rather than on the local boundary layer thickness. Given the similar response of different boundary layers (in terms of $U_e\,\delta_0/\nu$) to curvature of varying strength (as measured by δ_0/R), they proposed that boundary layers perturbed by strong convex curvature approach the same asymptotic state. In this state, they defined the limit of strong convex curvature to occur when $\delta_0/R \geqslant 0.05$. They also inferred that the severe reduction of the shear stress in the outer part of the mean shear layer, the nearly isotropic normal stresses, and the scaling with R means that the region of convex curvature limits the size of the anisotropic, stress-containing structures to less than the region of mean velocity gradient; the large eddies in the incoming boundary layer must then be 'destroyed or modified in such a way that the [upstream] history is lost' (Gillis & Johnston, 1983). They proposed that if this perturbed boundary layer were allowed to relax on a flat plate its recovery would show a dual nature: an outer region containing the isotropic and decaying debris of the upstream boundary layer, and an active inner layer where new turbulence is produced, which grows into the outer region in a manner similar to normal turbulent boundary layer growth.

A few experiments have also examined the initial relaxation from a curvature perturbation. Gillis & Johnston's work included a flat plate recovery length of $35\delta_0$–$40\delta_0$ after the end of curvature. Smits, Young & Bradshaw (1979) subjected a turbulent boundary layer to 30° of strong ($\delta_0/R \approx 0.2$) convex curvature and then

allowed it to relax on a flat plate in a mild favourable pressure gradient over a distance of approximately $60\delta_0$. Both studies showed that the stress levels suppressed by curvature were regenerated on the flat plate; stress ratios such as $a_1 \equiv -\overline{uv}/\overline{q^2}$ (where $\overline{q^2}$ is twice the turbulent kinetic energy) recovered to the upstream value within a few δ_0. Far enough downstream, however, the absolute stress levels were higher than in the upstream self-preserving layer (see, for example, figure 1). Thus, surprisingly, the long-term relaxation from stabilizing curvature resulted in increased turbulent mixing, compared to the unperturbed boundary layer.

Another interesting experiment was performed by Castro & Bradshaw (1976) who investigated the relaxation of a turbulent mixing layer from stabilizing curvature. The turbulent mixing layer turned through 90° of strong convex curvature ($\delta/R \approx 0.02$) and then relaxed asymptotically to the self-preserving state. As for the case of boundary layer flows, they found that stabilizing curvature reduced turbulence levels in the mixing layer and that the recovery to the unperturbed state was markedly non-monotonic. The Reynolds stresses, triple products, and other turbulence qualities showed significant overshoots near the centreline of the shear layer before decreasing towards the unperturbed levels. Again, the structure parameter a_1 recovered monotonically and fairly quickly. Castro & Bradshaw attributed the over-recovery of the turbulence intensities to the suppression of the triple products and therefore presumably to the suppression of the large eddies, which take time to regenerate after curvature is removed; the slow recovery of the large structures means that they cannot effectively redistribute the turbulence being regenerated near the centre part of the shear layer, at least initially.

In the present experiment, a turbulent boundary was turned through 90° of strong convex curvature ($\delta_0/R = 0.08$) and then allowed to relax on a flat plate. This work is an extension of that done by Gillis & Johnston; it differs from theirs in that the long-term evolution of the perturbed boundary layer was examined over an increased relaxation length ($\approx 90\delta_0$, versus $35\delta_0$–$40\delta_0$ in their flow), and in that different types of measurements are presented, beyond mean flow and Reynolds-averaged results, which attempt tc describe the structural changes in the relaxing boundary layer. In both studies, the pressure gradient was minimized to determine more easily the boundary layer relaxation from curvature effects. One complete set of measurements was made upstream of curvature in the unperturbed boundary layer, and this constituted a reference set. All other measurements were taken downstream of the curved region. No data were taken within the perturbation itself: this study is strictly limited to the relaxation of the boundary layer.

2. Experimental facility and instrumentation

The results were obtained in the subsonic, open-return wind tunnel shown in figure 2. A 1.0 mm diameter wire was used to trip the boundary layers on all four walls of the 0.15 m × 1.22 m working section. The test-wall boundary layer developed in a zero pressure gradient with a free-stream velocity of 31 m/s ($U_\infty/\nu = 2 \times 10^6\ \mathrm{m}^{-1}$) and a free-stream turbulence intensity of 0.3%. At a distance of 1.5 m downstream of the trip, the boundary layer had a Reynolds number based on momentum thickness Re_θ of 6000. At this point, the boundary layer was subjected to 90° of constant-radius strong convex curvature, with $\delta_0/R \sim 0.08$ ($\delta_0 = 22.7$ mm, $R =$ 300 mm). To isolate curvature effects from those due to pressure gradient, the wall opposite the test wall was contoured to minimize the test-wall pressure gradient. The

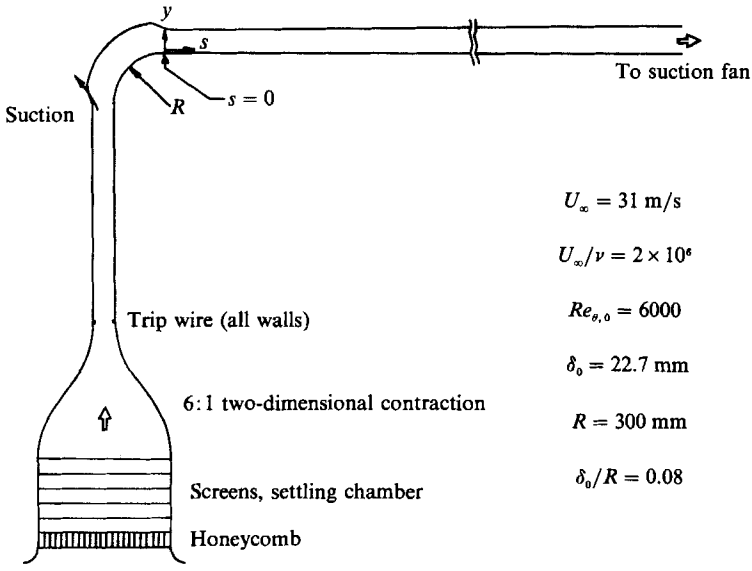

FIGURE 2. Wind tunnel schematic. The streamwise coordinate s is measured from the end of the curved section.

outer-wall boundary layer was removed by suction to prevent separation. At the exit from the curved section, the test-wall boundary layer was allowed to relax on a flat plate, again in zero pressure gradient, over a distance of 4.9 m.

The presence of the bend introduced a source of secondary flow from the sidewall boundary layers. This was minimized by the use of high-momentum, low-mass-flow-rate jets located on the sidewalls near the beginning of curvature, as first suggested by So & Mellor (1973). The spanwise variations in skin friction and Reynolds stress over the centre half of the span were small ($\pm 4\%$ and $\pm 10\%$, respectively). Furthermore, downstream of the bend, the terms in the two-dimensional momentum equation balanced to within $\pm 3\%$, and the flow was therefore judged acceptably two-dimensional.

Three different experiments were performed, called Case I, Case II, and Case III. The bulk of the work presented here relates to Case I, where the streamwise pressure distribution was as shown in figure 3. Within the bend, the pressure deviated significantly from its upstream reference value, and C_p varied by $\pm 0.09\%$. At one point near the bend exit, the magnitude of the pressure gradient parameter $\beta = (\delta^*/\tau_w)\, \mathrm{d}p/\mathrm{d}s$ was as large as 9. Although this indicates a strong pressure gradient, the strongest gradients are of short duration and of opposite sign, so that their integrated effect on the flow should be small. In the mean, the pressure gradient imposed during curvature appears to be significant only in the initial stage of recovery; the effects of curvature seem to last much longer. This point is discussed in §3.

A circular Pitot tube of 1.0 mm diameter was used to measure the total pressure in the boundary layer, and the skin friction was measured with Preston probes of diameter 1.0, 1.6, and 2.4, using the calibration suggested by Patel (1965).

The one-point turbulence measurements were taken using DANTEC 55P05 (normal-wire boundary layer) and 55P51 (crossed-wire) probes. The probes were modified so that the active wire lengths were reduced to 0.75 mm (length-to-diameter ratio of 150), and the spacing between crossed wires was reduced to 0.4 mm (29 in

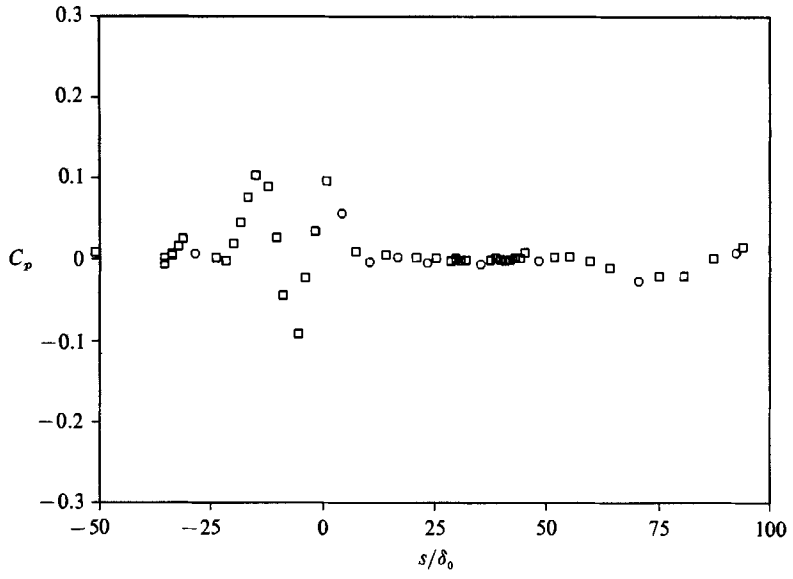

FIGURE 3. Streamwise static pressure distribution (Case I).

wall units) to minimize spatial resolution difficulties (see Alving 1988 for further details). The rake of wires for multiple-point turbulence measurements was provided by Steve Robinson of NASA Ames. It consisted of eight normal wires (of which six were used) spaced 0.5 to 1.0 mm apart in the direction normal to the wall, resulting in a total span of 5.5 mm. The probe tip was only 25 mm upstream of the shaft and the probe had a large cross-sectional area, raising some doubts about possible flow blockage. However, the spectra measured by the rake showed no abnormalities, and the two-point correlations derived from the rake measurements were similar to those obtained using a much more slender two-wire probe (constructed using DANTEC 55P01 probe bodies), so that blockage effects were inferred to be small.

DANTEC 55D01 and 55M10 constant-temperature anemometers were used, operating at overheat ratios of 0.7 with frequency responses of at least 65 kHz (as determined by the square wave test). The signals were filtered at 25 kHz with a fourth-order Butterworth filter (Ithaco, model 4213). The one-point signals were digitized at 2.5 and 50 kHz with a 12 bit A/D, LeCroy model LG8212A with a single 32 kByte 8800A memory module attached. The data taken at the lower frequency were used for long-time averages, while the higher frequency data were used for spectral decomposition. The rake data were digitized at 250 kHz using a 10 bit A/D, LeCroy model TD8210, with two memory modules.

For all of the one-point measurements, the wires were calibrated using a dynamic calibration scheme, as described by Perry (1982) and modified by Watmuff (1979) and Alving (1988). In brief, the small perturbation sensitivity of each wire was measured directly by applying a known velocity perturbation to the probe and measuring the resulting voltage perturbation. These perturbation data were used to evaluate the coefficients in a curve-fit of the flow velocity to the anemometer output voltage. The resulting uncertainties were estimated to be less than $\pm 3\%$ for $\overline{u^2}$, $\pm 5\%$ for $\overline{v^2}$ and $\overline{w^2}$, and $\pm 7\%$ for $-\overline{uv}$.

3. Mean flow results

The skin friction coefficients are shown in figure 4, and there appears to be generally good agreement among the various estimates of C_f. Two exceptions to this agreement are worth discussing. First, there is some scatter in the initial recovery region. This may be expected, since the Preston probe calibration is affected by pressure gradients. Patel (1965) correlated the errors in the inferred skin friction using the pressure gradient parameter Δ, where $\Delta = (\nu/\rho u_\tau^3)\,\mathrm{d}p/\mathrm{d}s$. Between $s/\delta_0 =$ 4 and 10, Δ was estimated at -0.006 or -0.007, and Patel's calibration suggests C_f

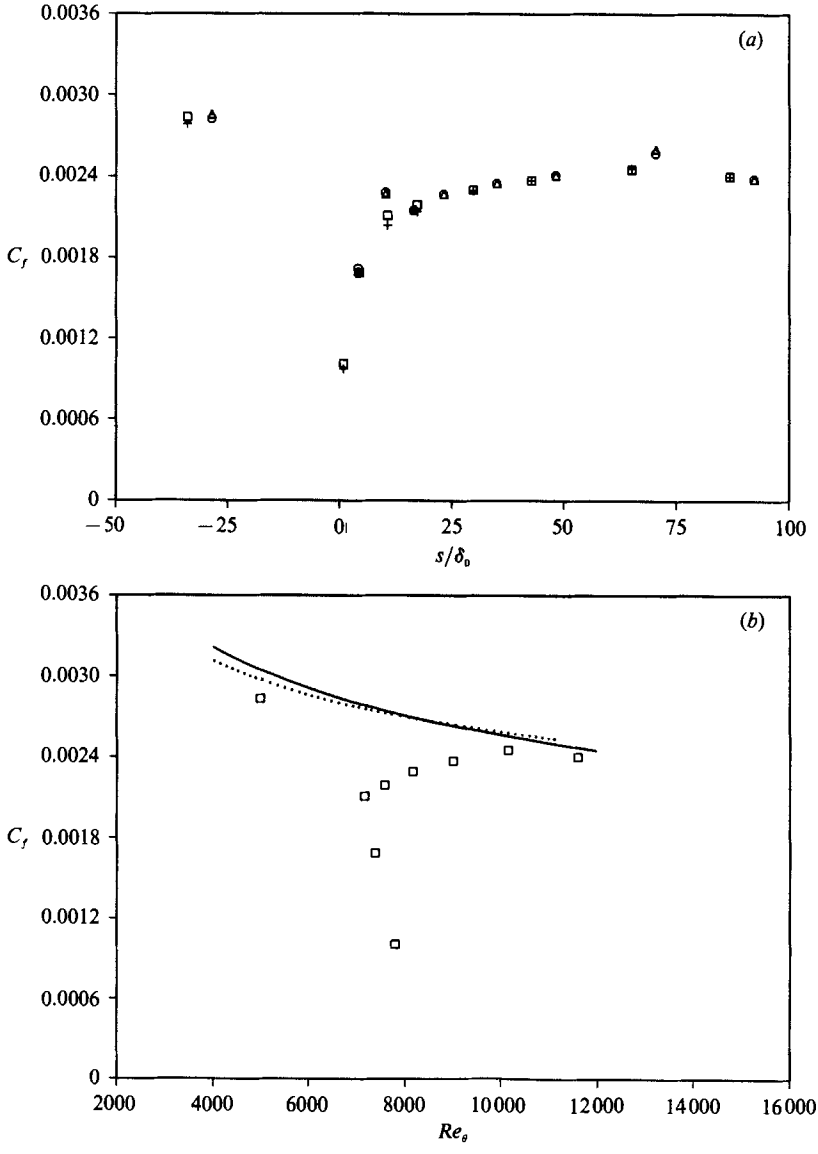

FIGURE 4. (*a*) Skin friction coefficient distribution (Case I): Clauser chart: □, Preston tube: +, $D = 1.0$ mm; △, $D = 1.6$ mm; ○, $D = 2.4$ mm. (*b*) Skin friction coefficient versus Re_θ (Case I): ——, Schlichting (1979); · · · · · · · · , Bradshaw, Ferris & Atwell (1967). Other symbols as in (*a*).

is over-estimated by 6% in this region. In the rest of the recovery, the pressure gradient was negligible.

Other than in the initial recovery region, the skin friction results only show scatter around $s/\delta_0 = 65$–70. These measurements were retaken several times, without discovering the source of the discrepancy. Three-dimensionality was probably not the cause, as no significant indication of secondary flow was found during tunnel qualification. One potential source of the discrepancy could be the slight favourable pressure gradient at this measuring station (see figure 3). The Reynolds stress behaviour also shows an anomaly (see §4) which may be due to this small pressure gradient.

Notwithstanding the difficulties in measuring skin friction, its recovery behaviour in unambiguous. At the bend exit, the low values of the skin friction reflect the stabilizing influence of convex curvature. Once the curvature is removed, the skin friction begins to recover and, initially, this recovery is quite fast; the skin friction doubles within $10\delta_0$. Subsequently, the recovery rate decreases, but C_f continues to increase through most of the recovery.

Because the skin friction for an unperturbed flat plate boundary layer is a function of Reynolds number, the degree of recovery is best expressed in terms of C_f versus Re_θ (figure 4*b*). In the early stage of recovery the boundary layer is obviously far from equilibrium, but in the later stage ($s/\delta_0 > 25$), the measured skin friction appears to approach the flat plate correlations asymptotically. Given the uncertainty in the flat plate correlations for C_f reported in the literature (see, for example, Smits, Matheson & Joubert 1983), it is difficult to say whether the last measured value has reached the flat plate level. In any case, the discrepancy, if it exists, is small.

There remains the question of how the skin friction results from different experiments can be compared. The Reynolds number, pressure gradient, and strength and duration of curvature can all vary, and it is not immediately obvious how these parameters may affect the recovery. Gillis & Johnston showed that within the bend curvature has an 'organizing' influence on the skin friction, in that boundary layers with different δ_0, (δ_0/R) and C_f at the beginning of the same curved test rig showed very similar skin friction behaviour within the curved region. To examine the effect of pressure gradient, two further tests were performed (Cases II and III). In Case II the outer wall was concentric with the inner wall, and in Case III the outer wall was contoured as described in §2. The resulting pressure gradients are shown in figure 5. Note that for Cases II and III, $U_e/\nu = 1.6 \times 10^6/\mathrm{m}$, compared with $2 \times 10^6/\mathrm{m}$ for Case I. For all three cases, the skin friction distributions are shown in figure 6, along with the results of Gillis *et al.* (1980) (90° turning, $\delta_0/R = 0.1$, $\mathrm{d}p/\mathrm{d}s$ small), Youssefmir (1982) (an extension of the Gillis & Johnston experiments), and Smits *et al.* (1979) (30° turning, $\delta_0/R = 0.2$, strong pressure gradients in the bend, mild favourable pressure gradient downstream). This plot shows that the initial level of C_f depends on the pressure gradient history; however, this effect is quickly erased, and by $s/\delta_0 \sim 25$ the recovery behaviour of all the different flows looks remarkably similar. From these results, it appears that the effect of pressure gradient within the bend is only important near the beginning of recovery. The curvature effects are much more long-lasting, and the pressure gradients experienced within the bend in this work should not affect the long-term recovery behaviour of the boundary layer.

The results shown in figure 6 have important implications for the potential of using convex curvature for drag reduction. The level of the skin friction in the relaxing boundary layer appears to be independent of the skin friction level at the end of the bend, except in the initial recovery region. Thus, although a short region of adverse

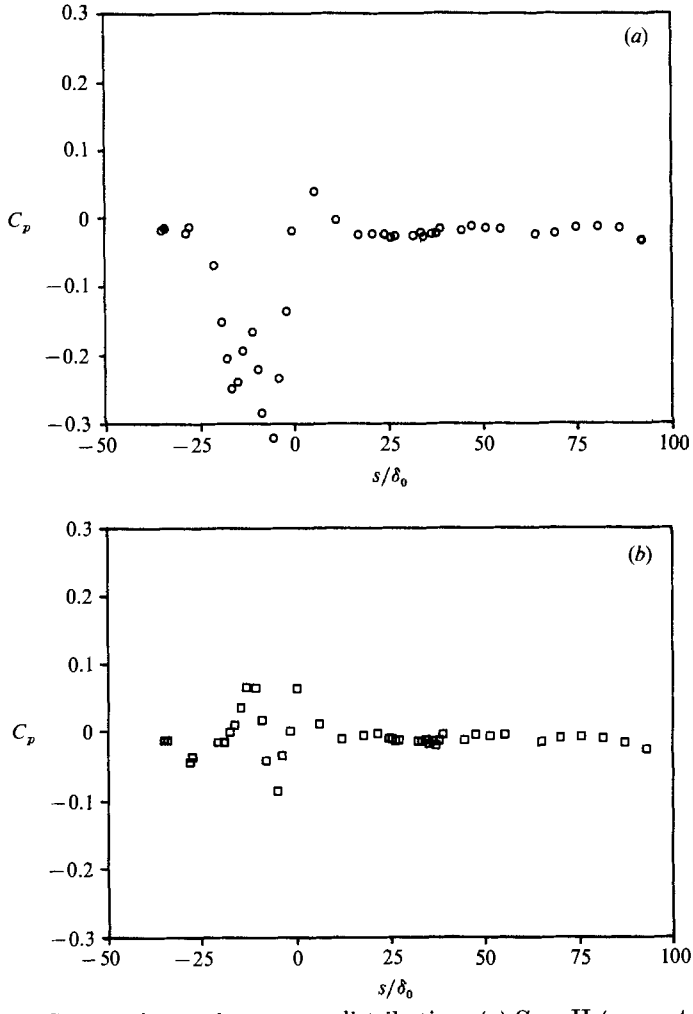

FIGURE 5. Streamwise static pressure distribution: (*a*) Case II (concentric outer wall); (*b*) Case III (contoured outer wall).

pressure gradient at the end of the curved section can initially decrease the skin friction (consider Case I), there is not a lasting benefit for drag reduction on the flat plate.

Initially, it was surprising to find that s/δ_0 scaling collapsed the skin friction results of several investigators, because the results of Gillis & Johnston implied that the large-scale 'history containing' eddies were removed by stabilizing curvature, and that the effective (stress-containing) boundary layer thickness decreased in the bend. In that case, the size of the upstream boundary layer should be irrelevant to the recovery process. However, as δ_0 depends on the Reynolds number, this scaling may just reflect the Reynolds number dependence of the recovery.

The mean velocity profiles are plotted in figure 7. The logarithmic law of the wall is expressed in terms of $u^+ \equiv U/u_\tau$ and $y^+ \equiv yu_\tau/\nu$ as

$$u^+ = \frac{1}{\kappa} \ln y^+ + C,$$

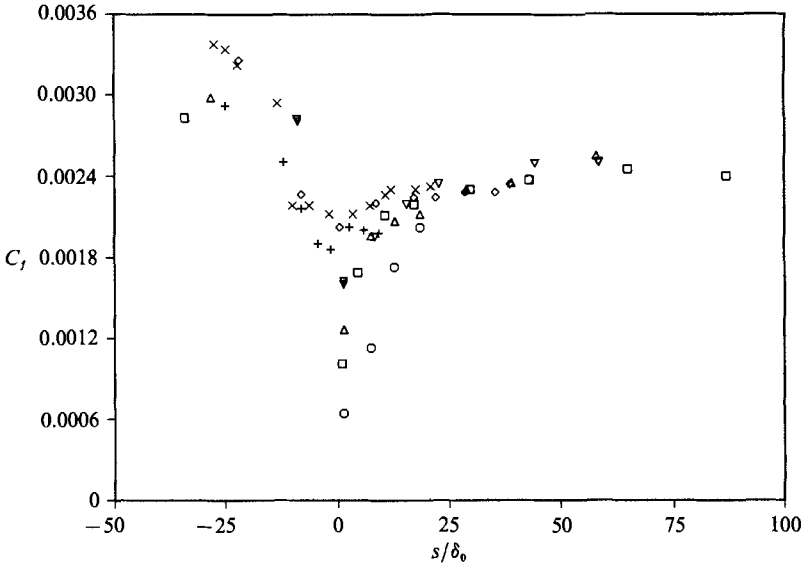

FIGURE 6. Skin friction coefficient distribution: □, Case I, ○, Case II; △, Case III; + and X, Gillis & Johnston (1983); ◇, Youssefmir (1982); ▽, Smits *et al.* (1979).

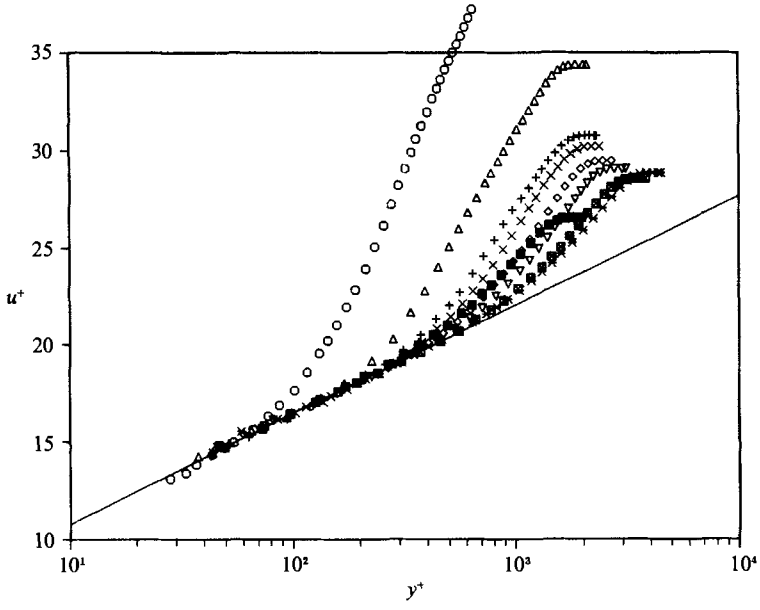

FIGURE 7. Mean velocity profiles, inner scaling: ■, upstream reference; ○, $s/\delta_0 = 0.8$; △, 4; +, 11; ×, 17; ◇, 29; ▽, 42; ⊠, s/δ_0; *, 87.

with $\kappa = 0.41$ and $C = 5.2$ (these constants were suggested by deBrederode & Bradshaw (1974) as the best fit to the published data). At the bend exit, the effect of the boundary layer perturbation is shown by the short extent of the logarithmic region and by the large wake factor. Once the curvature is removed, the velocity profile initially changes quickly; between the two stations at $s/\delta_0 = 2$ and 4, the wake factor decreases by 50%. The recovery rate remains high for the first $10\delta_0$. With

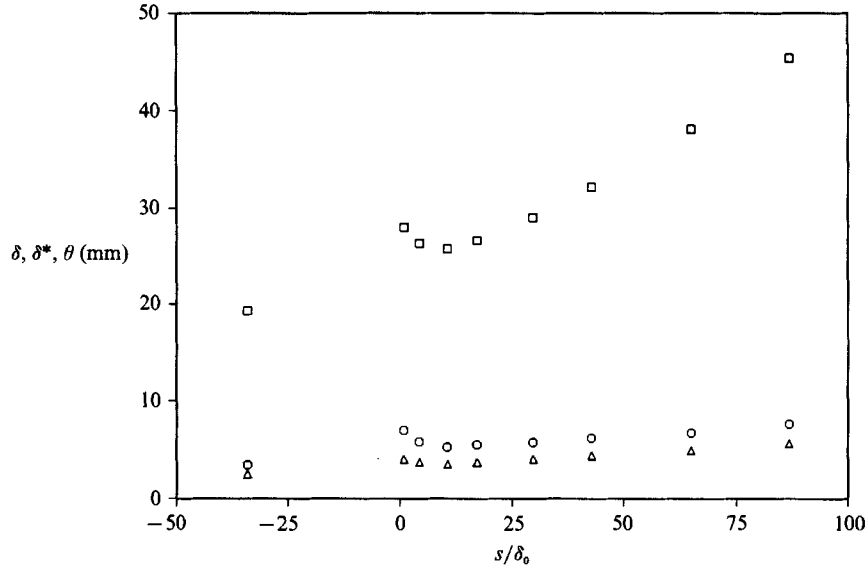

FIGURE 8. Distributions of: □, boundary layer thickness δ; ○, displacement thickness δ^*; △, momentum thickness θ.

further recovery, the Coles wake factor π asymptotically approaches a constant level of 0.76; this value is slightly higher than the upstream reference level of 0.68.

At the bend exit the extent of the logarithmic region is small, but with streamwise recovery the log region grows, and it relaxes to its upstream level after only $s/\delta_0 = 25$. This implies that the inner and outer regions have reached some sort of self-preserving balance after $25\delta_0$. By integrating the mean velocity profiles, it can be shown that during the initial $\sim 12\delta_0$ of recovery the boundary layer mass flux remains approximately constant; that is, no new mass is entrained into the boundary layer. The lack of mass entrainment may be partly due to the favourable pressure gradient for $s/\delta_0 < 8$, and this may partially account for the differences in the initial recovery behaviour measured by Gillis *et al.* (1980). In their work the pressure gradient was practically zero throughout the bend, in contrast to the relatively strong pressure gradients seen within the bend in the present experiment (figure 3). They found that the boundary layer did not regain fullness for $20\delta_0$ after the end of curvature, and that the boundary layer entrainment did not go to zero as it does here.

All the boundary layer thicknesses (δ, δ^*, θ) increase through the bend, and then display a dip in the initial recovery region (figure 8). This dip is not an indication of a loss of mass flux m from the boundary layer [where $m = (\rho U_e (\delta - \delta^*)]$; rather, it indicates a redistribution of the mass flux within the boundary layer. This effect was also seen in the shape factor H and Clauser parameter G, which take large values at the exit from the bend. During the first $\sim 10\delta_0$ after the end of curvature, H, and G recover approximately 75% of the way to their flat plate values. With increasing streamwise distance, the recovery contines but at a much slower rate. The final levels of H and G are 1.35 and 7.54, compared with their upstream levels of 1.4 and 7.53.

Hence, the mean flow recovery process is initially quite fast, showing large increases in the skin friction, the shape factor, and the extent of the logarithmic region, a similar decrease in the wake factor, and a regrowth in the fullness of the

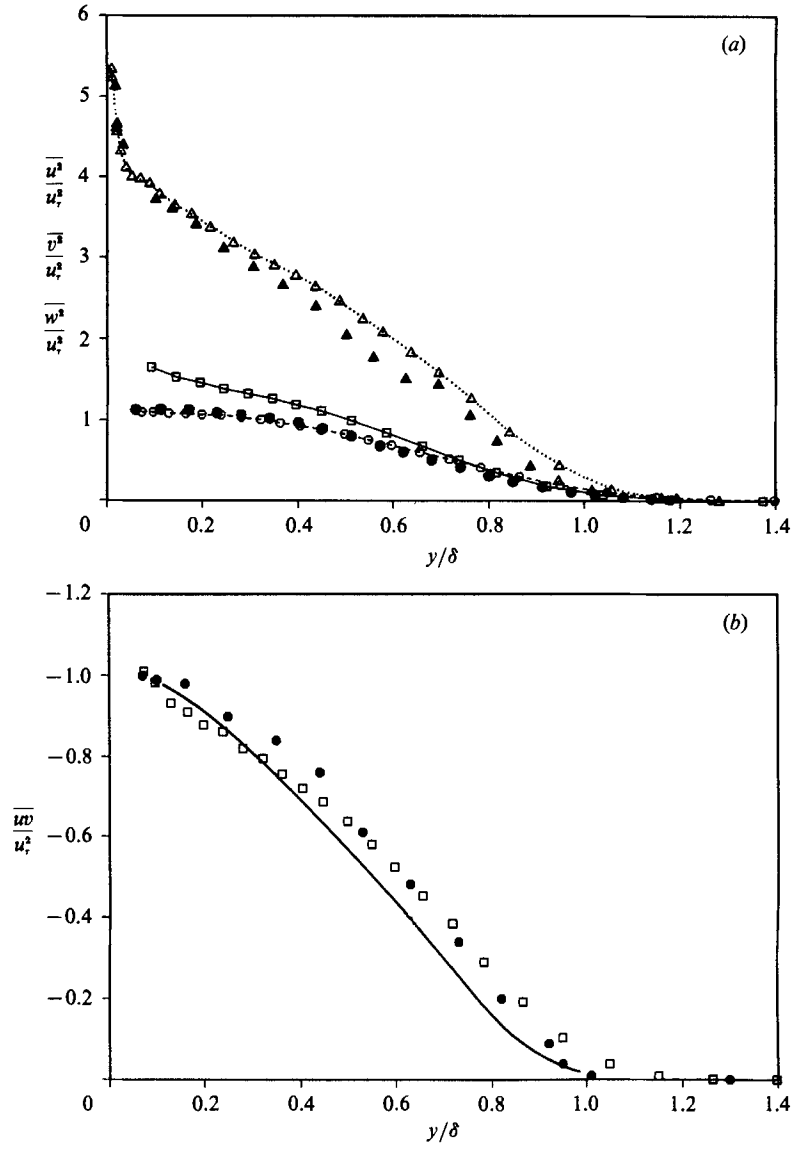

FIGURE 9. (*a*) Normal stresses in the upstream boundary layer: △, $\overline{u^2}/u_\tau^2$; □, $\overline{w^2}/u_\tau^2$; ○, $\overline{v^2}/u_\tau^2$. Filled in symbols are from Erm *et al.* (1987) at $Re_\theta = 5010$. (*b*) Shear stress in the upstream boundary layer. Filled in symbols from Erm *et al.* (1987). Solid line from Klebanoff (1955).

mean velocity profile. This stage lasts approximately $10\delta_0$ after the end of curvature, and pressure gradient effects may be important here. Subsequently, the mean flow relaxation continues at a decelerated rate, and the flat plate behaviour is approached asymptotically. At the last measuring station the mean velocity profiles and the integral parameters appear fully recovered.

4. Turbulence results

The three normal stresses ($\overline{u^2}$, $\overline{v^2}$, $\overline{w^2}$) and the shear $-\overline{uv}$ are plotted in figure 9 for the upstream boundary layer ($\overline{uw}$ was close to zero, and $\overline{vw}$ was not measured). The

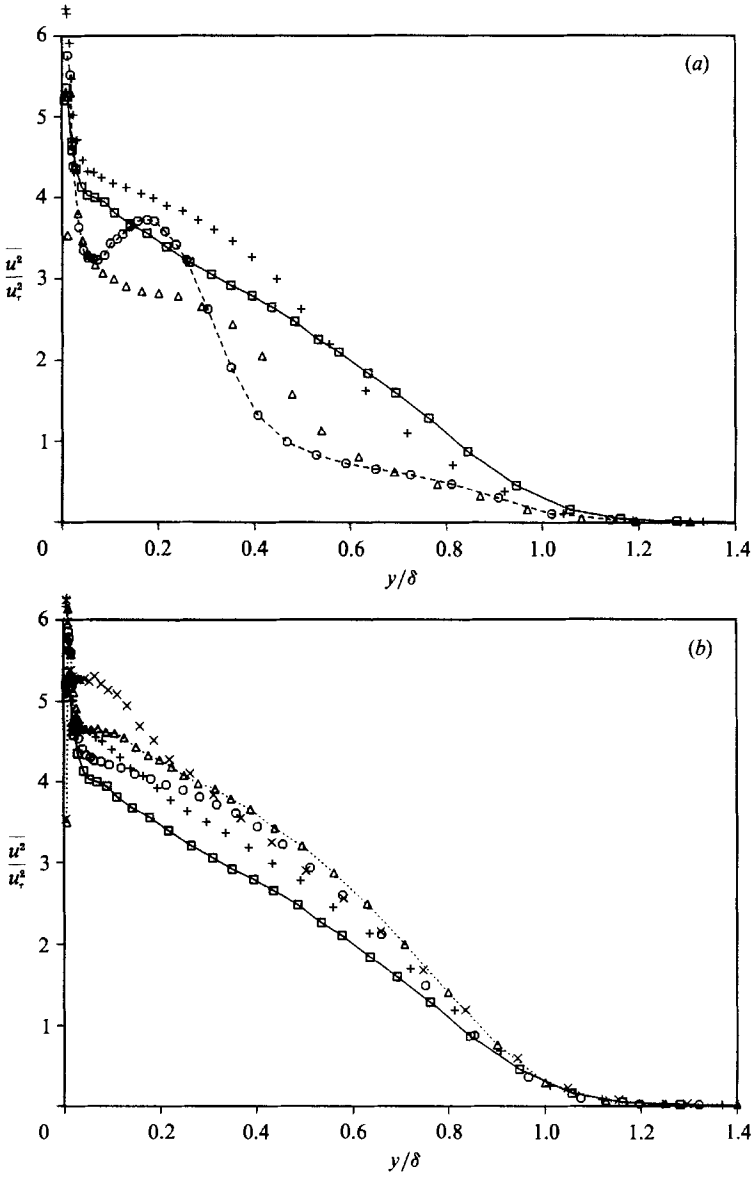

FIGURE 10. Relaxation behaviour of the streamwise component of the turbulence kinetic energy. (*a*) Initial recovery: □, upstream reference; ○, $s/\delta_0 = 4$; △, $s/\delta_0 = 11$; +, $s/\delta_0 = 17$; (*b*) later recovery: □, upstream reference; ○, $s/\delta_0 = 29$; △, 42; +, 64; ×, 87. Lines for visual aid only.

measurements of Erm, Smits & Joubert (1987) at a comparable Reynolds number are also shown, and the two sets of data agree well. This agreement is further indication that the upstream reference boundary layer was close to a 'standard' two-dimensional boundary layer. The notion of 'universal' boundary-layer characteristics was questioned by Smits *et al.* (1977), who demonstrated that in fact significant discrepancies exist amongst widely accepted correlations for C_f, H, G and wake factor π. The results presented here for the recovering boundary layer cast further doubt on the existence of a universal flat plate flow (see §6).

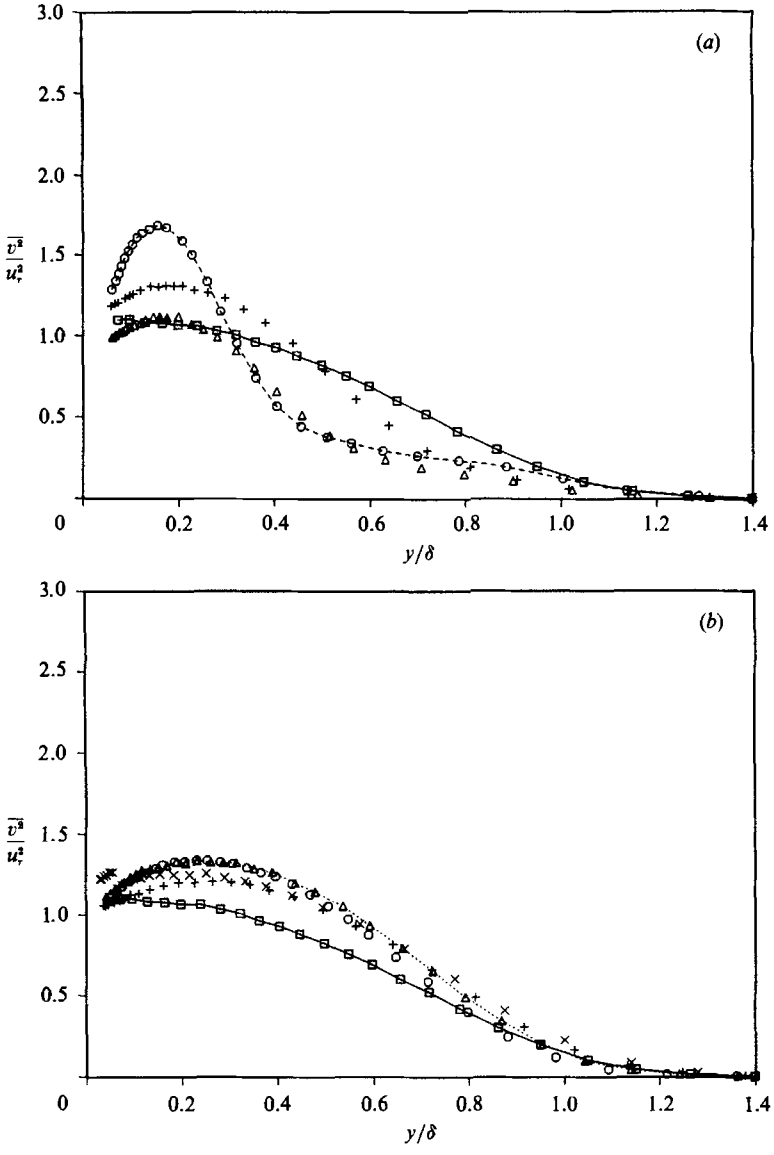

FIGURE 11. Relaxation behaviour of the normal component of the turbulence kinetic energy: (*a*) initial recovery (symbols as in figure 10*a*); (*b*) later recovery (symbols as in figure 10*b*). Lines for visual aid only.

Reynolds stress measurements in the relaxing boundary layer at the first three streamwise locations are plotted in figure 10 I(*a*)–13(*b*).

As seen from the near-wall measurements of $\overline{u^2}/u_\tau^2$, the flow closest to the wall recovers fastest, and in outer coordinates the perturbed profiles look very similar to the upstream case. This is not surprising, since response times are shortest near the wall. Away from the wall, the initial recovery from convex curvature is in terms of a stress 'bore', a distinctly defined region of elevated stress moving away from the wall with increasing downstream distance. This bore occurs in all components of the normal stress and in the shear $-\overline{uv}$, and its formation can be explained in terms of the

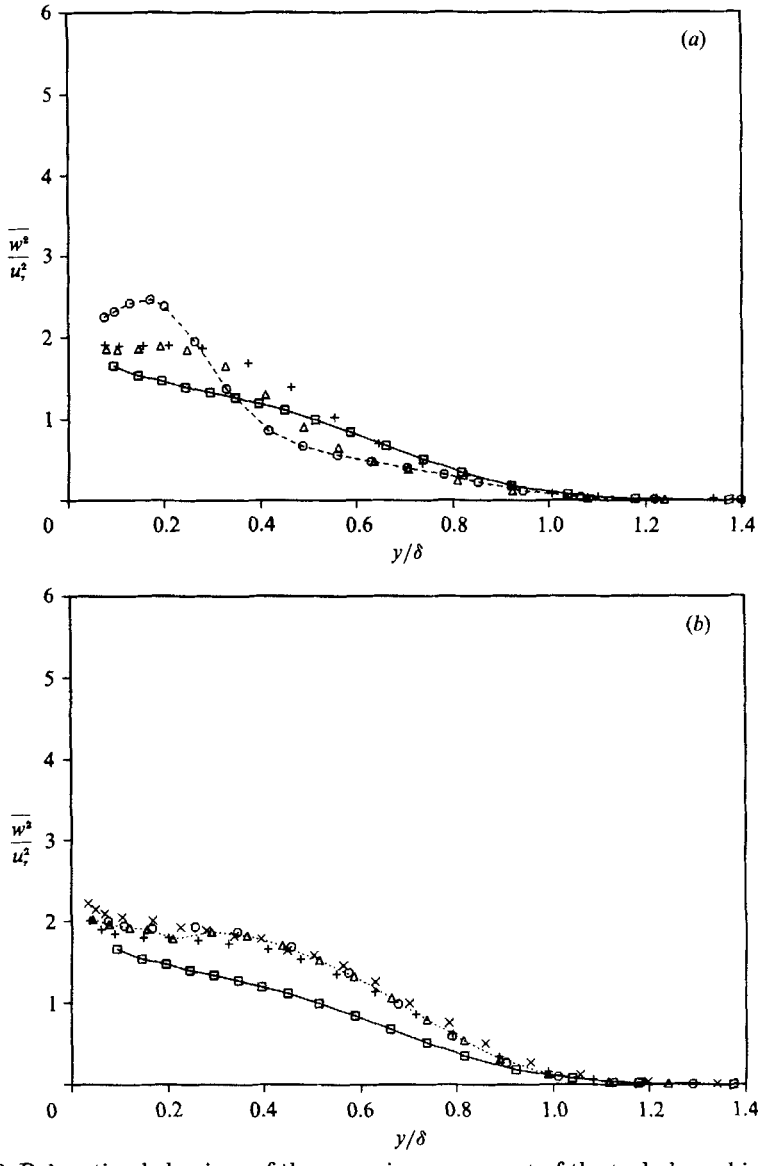

FIGURE 12. Relaxation behaviour of the spanwise component of the turbulence kinetic energy: (*a*) initial recovery (symbols as in figure 10*a*); (*b*) later recovery (symbols as in figure 10*b*). Lines for visual aid only.

Reynolds stress transport equations, which express the coupling between the stresses. At the end of the convex curvature, the mean shear $\partial U/\partial y$ is reduced at the wall and therefore increased away from the wall, relative to an unperturbed profile. The normal stress $\overline{v^2}$ is reduced but still important at the end of the curvature. Once the stabilizing effect of convex curvature is removed, the production term $\overline{v^2}\,\partial U/\partial y$ in the shear stress transport equation causes a regrowth of $-\overline{uv}$; this in turn causes an increase in (twice) the turbulent kinetic energy $\overline{q^2}$ via the production term $-\overline{uv}\,\partial U/\partial y$. Thus, although convex curvature causes a decrease in turbulent mixing, it

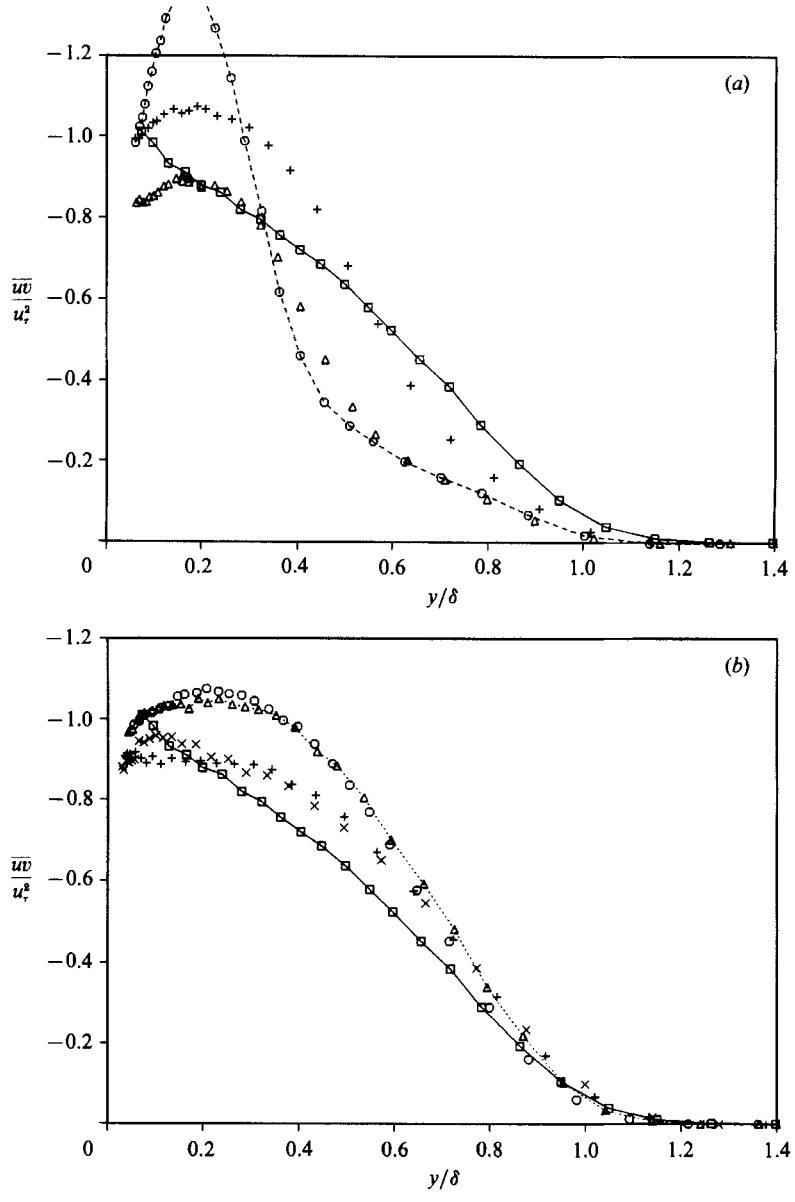

FIGURE 13. Relaxation behaviour of the shear stress: (*a*) initial recovery (symbols as in figure 10*a*); (*b*) later recovery (symbols as in figure 10*b*). Lines for visual aid only.

distorts the boundary layer in a manner that provides the capability for the regeneration of the turbulence once this stabilizing influence is removed.

As the boundary layer relaxation progresses on the flat plate, the stress bore initiated at the end of curvature thickens and moves away from the wall. Before $30\delta_0$ the stress levels are elevated across the whole boundary layer. The maxima in the Reynolds stress plots correspond to the regions of maximum slope in the profiles of the transport velocities $V_r = \overline{uv^2}/\overline{uv}$ and $V_q = \overline{q^2 v}/\overline{q^2}$ (see Alving 1988 for details), indicating that the high stress levels are accompanied by an increase in turbulent

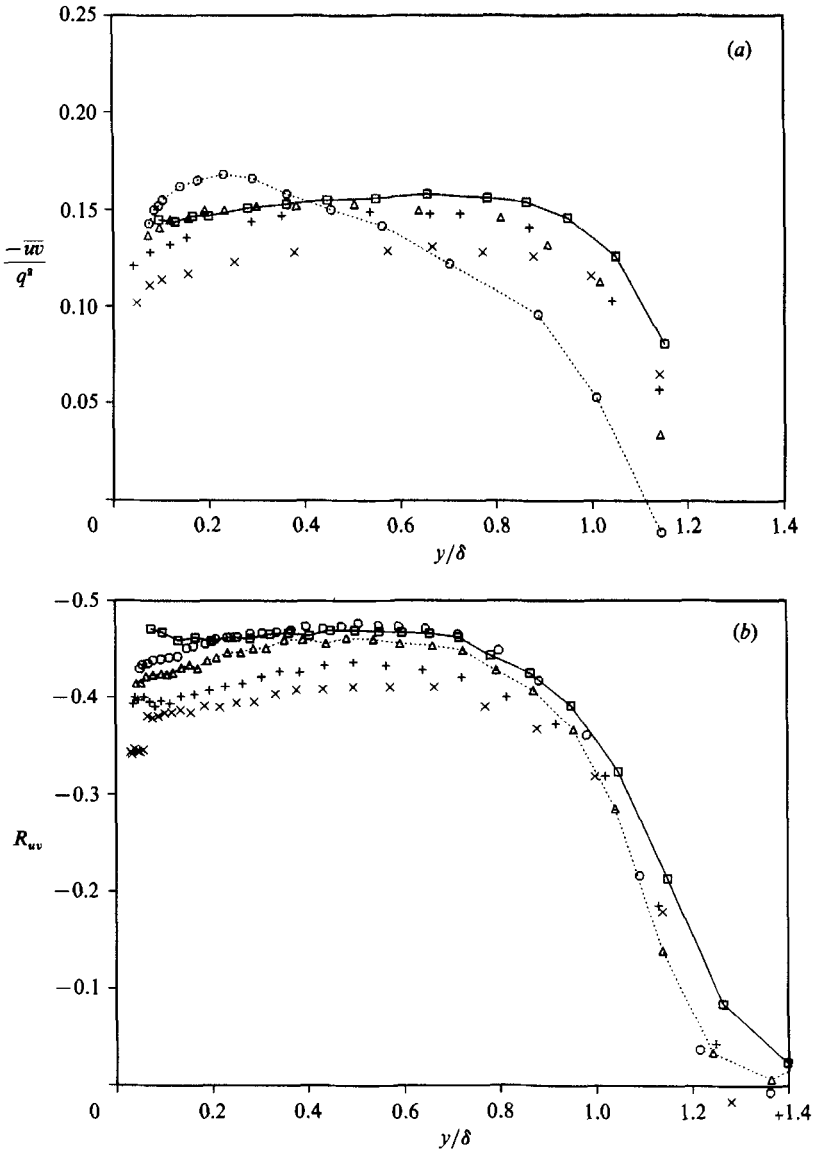

FIGURE 14. (*a*) Relaxation behaviour of the structure parameter $a_1 \equiv -\overline{uv}/\overline{q^2}$: □, upstream reference; ○, $s/\delta_0 = 4$; △, 17; +, 42; ×, 87. (*b*) Relaxation behaviour of the shear correlation coefficient $R_{uv} \equiv \overline{uv}/u_{\rm rms}\, v_{\rm rms}$: □, upstream reference; ○, $s/\delta_0 = 29$; △, 42; +, 64; ×, 87. Lines for visual aid only.

transport for $-\overline{uv}$ and $\overline{q^2}$. Thus, the production terms (for example, $-\overline{uv}\partial U/\partial y$) generate the elevated stress levels, and the turbulent transport terms (for example, $\partial(\overline{q^2 v})/\partial y$) lead to a stress bore where the outer edge of the elevated stress region 'diffuses' outwards with increasing downstream distance.

In spite of the severely distorted stress profiles in the initial recovery, the normal stresses and the shear stress have very similar recovery behaviours. It is not surprising, therefore, that ratios of these stresses show very little difference from the upstream reference boundary layer. Figure 14 shows the ratio $a_1 \equiv -\overline{uv}/\overline{q^2}$ and the shear correlation coefficient $R_{uv} \equiv \overline{uv}/u_{\rm rms}\, v_{\rm rms}$. The former is slightly more

distorted in the initial recovery, especially in the outer part of the boundary layer where the shear $-\overline{uv}$ is low. Gillis & Johnston (1983) postulated that the outer layer contains the isotropic decaying debris of the upstream large eddies; this contributes to $\overline{q^2}$ but not to $-\overline{uv}$, resulting in low a_1. However, a_1 recovers quickly, and neither a_1 nor the anisotropy ratio $\overline{u^2}/\overline{v^2}$ shows a severe perturbation comparable with those of the absolute stress levels.

The disappearance of the pronounced stress bore is taken to mark the end of the first stage of recovery.

The Reynolds stress profiles in the second and third stages of relaxation are shown in figures 10(*b*–113(*b*). In the second stage of recovery ($25\delta_0 < s < 45\delta_0$), where the mean velocity profiles are still recovering, the rate of change slows, but the stress levels continue to increase uniformly above their self-preserving levels. In the third stage ($s > 43\delta_0$), where the skin friction and velocity profiles have fully recovered, the stress levels begin to decrease; this is first seen at $64\delta_0$ and continues at $87\delta_0$. The only exception is in the streamwise component of the normal stress; especially near the wall, $\overline{u^2}$ actually increases at the last measuring station. This may be caused by the slight adverse pressure gradient at this location.

The third stage of recovery occurs at a considerably slower rate than the earlier stages, and differences between the last two measured profiles are slight, although they are separated by $23\delta_0$. Perhaps the elevated stresses would eventually return to 'normal' flat plate levels, given a long enough recovery length. However, the extremely slow rate of change of the stress profiles in the third stage of recovery implies that the driving force for this return is slight. For example, the transport velocities at the last measuring station looked very similar to the upstream flat plate profile.

The far downstream behaviour of the 'structure parameter' a_1 shown in figure 14 (*a*) is somewhat surprising. Although at $s/\delta_0 = 17$ (near the end of the first stage) the distribution of a_1 looks very much like that of the upstream profiles, its level has fallen across the boundary layer by the last measuring station. The shear correlation coefficient R_{uv} (shown in figure 14 (*b*) for the later recovery) has a similar behaviour in both the initial and the far downstream recovery. The anisotropy ratio, however, remains quite like the upstream profile. Thus, the relative magnitudes of $\overline{u^2}$ and $\overline{v^2}$ are comparable with the unperturbed case, while $-\overline{uv}$ is relatively less. Although these downstream charges in a_1 and R_{uv} are first seen near a region of slight pressure gradient, it is not likely that such a weak change in pressure would cause significant changes in a_1 and R_{uv}. These altered stress ratios may be a subtle indication of a fundamental change in the structure of the large-scale vorticity, although the measurements presented in §5 do not reflect this structural change. Inaccurate measurements of u and v could distort these ratios, but with the dynamic calibration technique used here the relatively small errors in $\overline{u^2}$, $\overline{v^2}$, $\overline{w^2}$, and $-\overline{uv}$ could not account for the 20% drop in a_1. In addition, a few repeated measurements near the wall in the last downstream station confirmed the results presented here. Thus, these trends for a_1 and R_{uv} appear to be real.

To summarize, the initial regrowth of the turbulence levels suppressed by the curvature occurs through a stress bore which is generated near the wall and carried outward by turbulent transport. In spite of the distortion this bore causes in the absolute stress levels, the various stresses change in a similar manner; therefore the stress ratios are not severely perturbed, and they recover quickly and monotonically. In the second stage of recovery, the bore has grown to fill the entire shear layer; however, the stress levels continue to rise, at a decreased rate, above the upstream

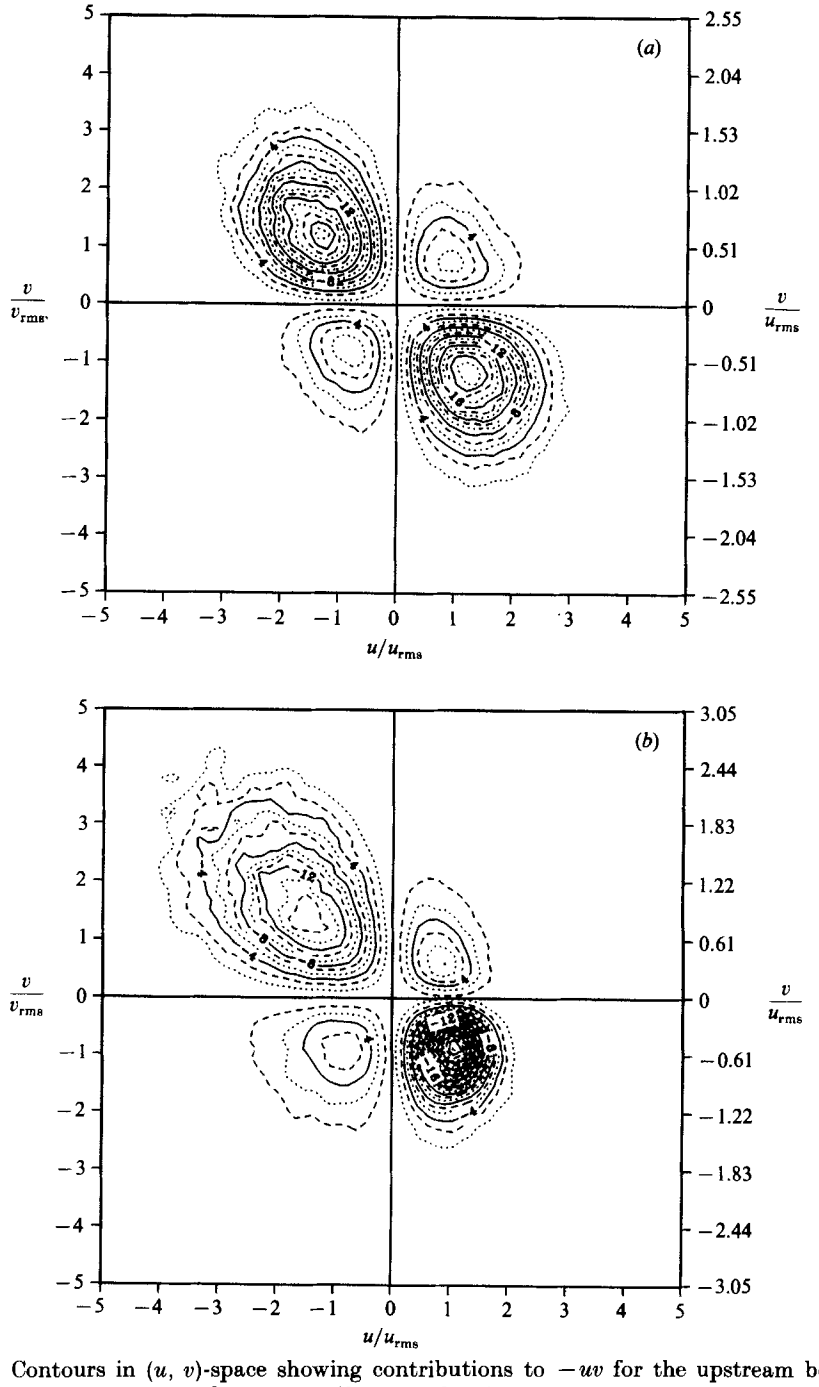

FIGURE 15. Contours in (u, v)-space showing contributions to $-uv$ for the upstream boundary layer: (*a*) $y/\delta = 0.1$; (*b*) $y/\delta = 0.7$.

levels. The third stage is marked by a drop in the stress levels, but the recovery rate is so slow that only a slight difference is measured over the last $23\delta_0$. The implication is that the eventual recovery to the upstream level would take a significantly longer relaxation length. In addition, the relative distribution of the components of the Reynolds stress tensor is distorted, as indicated by the decreasing level of a_1.

Relative to the self-preserving layer, there is less shear stress, given the level of turbulent kinetic energy. Thus, the Reynolds stress measurements indicate that, $87\delta_0$ after the end of curvature, the boundary layer is still quite different from the upstream self-preserving layer, both in the magnitude and in the distribution of the turbulent stresses. Clearly a very long distance would be required to complete the recovery process. This is in contrast to the mean flow behaviour, which does not look significantly different from the unperturbed case at the last measuring station.

To investigate the relaxation behaviour further, the higher-order moments were examined, along with the u–v statistics using the quadrant technique (Lu & Wilmarth 1973). The spectral content of the turbulence was also determined.

In the unperturbed boundary layer, statistical analysis confirms the results of earlier works. The velocity fluctuations are fairly Gaussian in the inner layer, whereas very close to the wall and near the outer edge of boundary layer the fluctuations depart from a Gaussian probability distribution. In the outer layer the large fourth-order moment (flatness) implies a highly intermittent signal, attributed to the entrainment of free-stream fluid by the large-scale boundary layer structure. Quadrant analysis shows that, in the inner (Gaussian) part of the layer, activity in Quadrant 2 (u negative, v positive) and Quadrant 4 (u positive, v negative) is equally probable and contributes almost equally to the shear stress $-uv$ (figure 15). With increasing distance from the wall Quadrant 2 outflow events become less probable, while simultaneously contributing more to the shear stress, with the converse true for Quadrant 4 events. Thus, the outer structure of the undisturbed boundary layer is characterized by the importance of energetic outflow events.

The statistics showed that in the initial relaxation from curvature, the low stress levels in the *outer* part of the boundary layer correspond to Gaussian-like velocity fluctuations typical of the *inner* layer in the undisturbed case (figure 16). The flatness was quite reduced, implying a reduction in the outer layer intermittency. In addition, the Quadrant 2 events are less dominant in determining the shear stress. (A suppresion in Quadrant 2 (outflow) events is consistent with the stabilizing effect of convex curvature.) These indications imply that the anisotropic large-scale structures are destroyed or at least weakened by convex curvature.

In the inner part of the layer, the Reynolds stress bore is related, but not identical, to areas of distortion in the p.d.f.'s. The leading edge of the stress bore corresponds to a region of non-Gaussian u- and v-fluctuations, and the sharp gradient of the bore is in the region of energetic outflow events. Thus, the bore may indicate the size of the largest structures regrowing from the wall. The elevated stress levels themselves do not indicate distortions in the p.d.f.s.

By the point where the stress bore fills the whole boundary layer, the distribution of velocity fluctuations in (u, v)-space looks very similar to that in the unperturbed boundary layer. Presumably, the large-scale structures have regrown to fill the entire shear layer. The elevated stress levels which persist far downstream are therefore not associated with distortions in (u, v)-space. This is reflected in the similarity of the anisotropy ratio between the upstream and downstream boundary layers, as noted earlier.

Spectral decomposition shows that, for a given streamwise location, the spectra scale on the local broad-band turbulence level and a fixed time-scale, δ/U_e. Surprisingly, this scaling holds even for the most severely perturbed boundary layer near the exit from the bend (see figure 17).

In comparisons between different streamwise locations, the major differences between the upstream reference and the recovering layers are in the low-frequency part of the spectra, implying differences in the large-scale boundary layer structure.

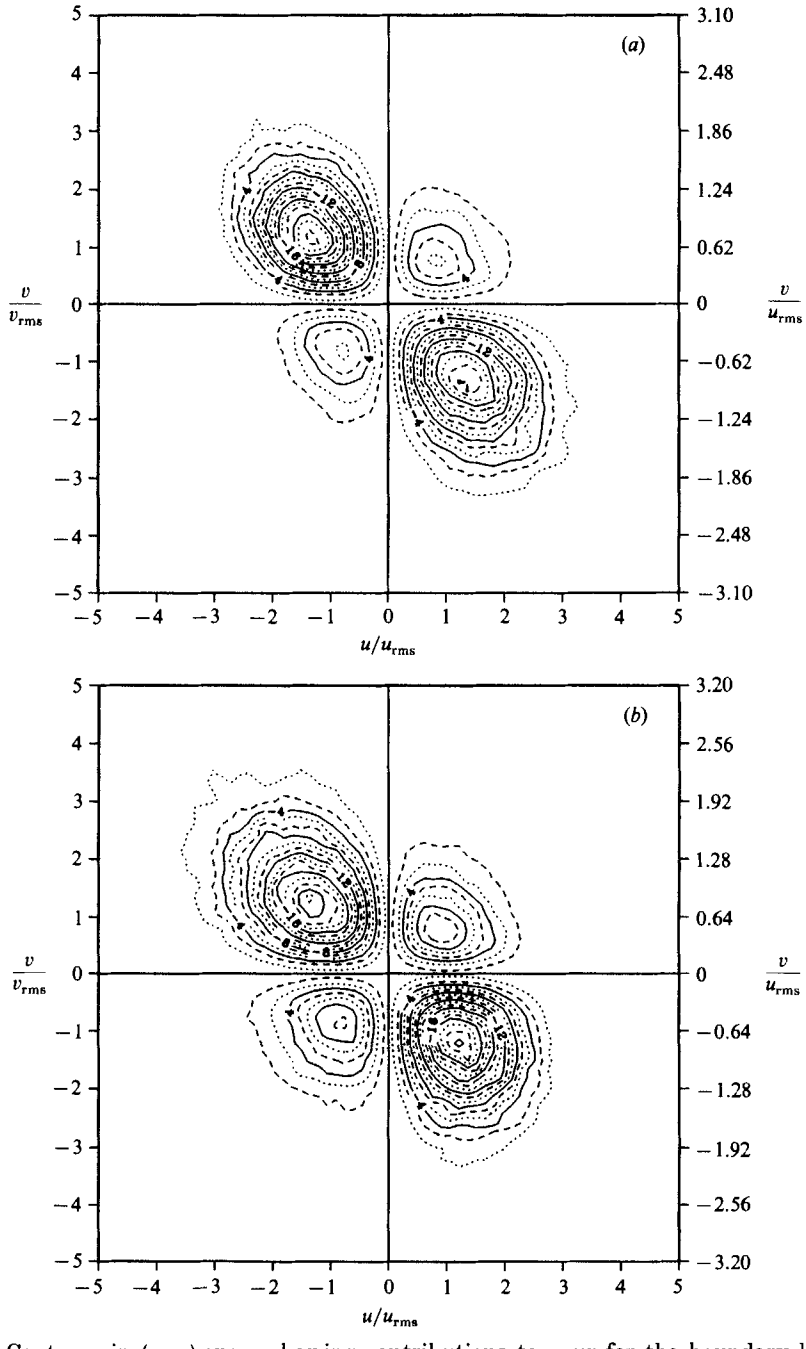

FIGURE 16. Contours in (u, v)-space showing contributions to $-uv$ for the boundary layer just downstream of curvature $(s/\delta_0 = 4)$ for $y/\delta = 0.7$.

At the exit from the bend the low-frequency component is suppressed near the wall and the low-frequency parts of the $\overline{v^2}$ and $\overline{w^2}$ spectra regrow before the $\overline{u^2}$ spectra. At the other stations, all three components of the turbulence kinetic energy regrow together, and far downstream the low-frequency contributions of all components are significantly elevated.

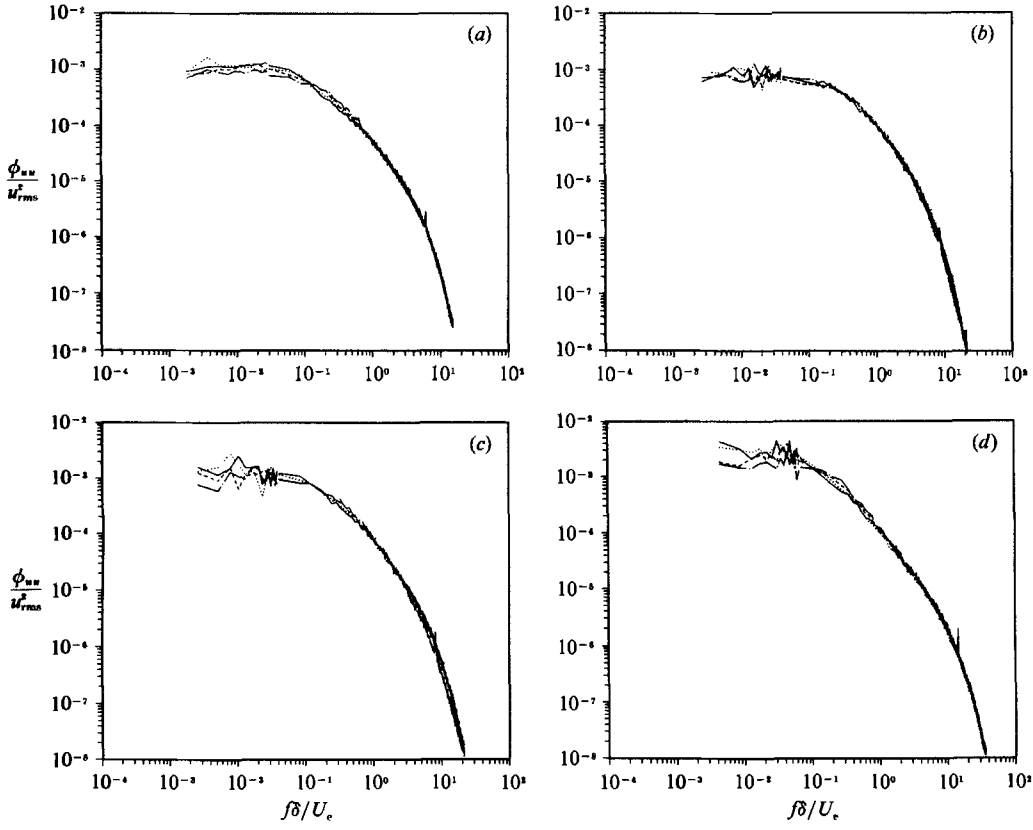

FIGURE 17. Power spectral density non-dimensionalized by the turbulence intensity, as a function of frequency non-dimensionalized by outer layer variables. For each station: ——, $y/\delta = 0.1$; · · · · · · ·, $y/\delta = 0.2$; - - - - - -, $y/\delta = 0.4$; ——·——, $y/\delta = 0.7$. (*a*) upstream; (*b*) $s/\delta_0 = 4$; (*c*) $s/\delta_0 = 17$; (*d*) $s/\delta_0 = 87$.

Spatial integration effects prevented a detailed investigation of the higher frequency range. However, all of the spectra appear to approach a universal curve in the inertial subrange, implying that the regrowth of the Reynolds stresses does not disturb the 'universal' part of the spectral distribution.

5. Multiple-point measurements

Large-scale coherent structures are believed to be important for turbulent transport in unperturbed boundary layers; furthermore, convex curvature appears to affect these structures dramatically. Simultaneous multiple-point measurements were therefore made to provide information about these structures in the unperturbed and recovering boundary layer.

Data were taken at several streamwise locations (upstream and at $s/\delta_0 = 3, 46, 91$) using a rake of six normal wires separated in the direction normal to the wall; the distance between the top and bottom wire was 5.5 mm. The probe was transversed from near the wall to beyond the edge of the boundary layer.

Cross-correlations $R_{AB}(\tau;\xi)$ were calculated for various pairs of the six wires, and this information was interpreted in terms of a large-scale 'structure angle' θ defined by Spina & Smits (1987). The concept is illustrated in figure 18. Consider a large-scale

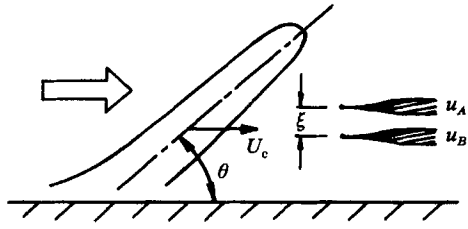

FIGURE 18. Schematic to illustrate definition of θ.

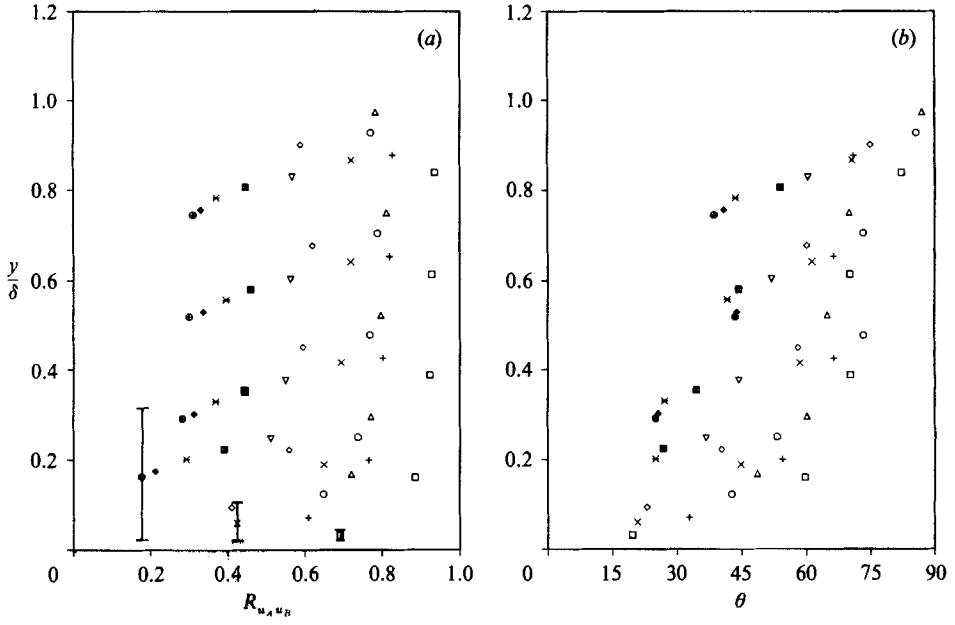

FIGURE 19. Unperturbed boundary layer. (*a*) Peak values of the cross-correlation; (*b*) average structure angle as a function of ξ/δ. Bars in (*a*) indicate span of wires for several ξ/δ. Other lines for visual aid only: □, $\xi/\delta = 0.023$; ○, 0.046; △, 0.049; +, 0.055, ×, 0.078; ◇, 0.10; ▽, 0.11; ⊠, 0.16; *, 0.21; ◇, 0.26; ⊕, 0.28.

structure, inclined towards the wall at some characteristic angle θ, convecting downstream at a velocity U_c. If the structure is large enough to span both wires, the velocity signal resulting from this structure will be measured first by the wire farther from the wall and, at a later time, by the wire closer to the wall. The peak in the broad-band cross-correlation, $R_{AB}(\tau;\xi)$, determines the time delay for which the outputs from the two wires are, on the average, most similar. Along with U_c and ξ (wire separation) this time delay τ_{max} can be converted to the average structure angle, θ:

$$\theta = \arctan\left[\frac{\xi}{U_c \tau_{max}}\right].$$

Of course, some estimate must be made for the convection velocity. In this work we assumed $U_c = 0.8U_e$; however, the choice of U_c is not critical to the results presented here. For instance, a 10% change in U_c results in only a 3° change in θ (maximum), which is less than the scatter in the data.

The peak in the cross-correlation and the average structure angle are plotted versus y/δ in figure 19, and both plots show a strong dependence on wire separation.

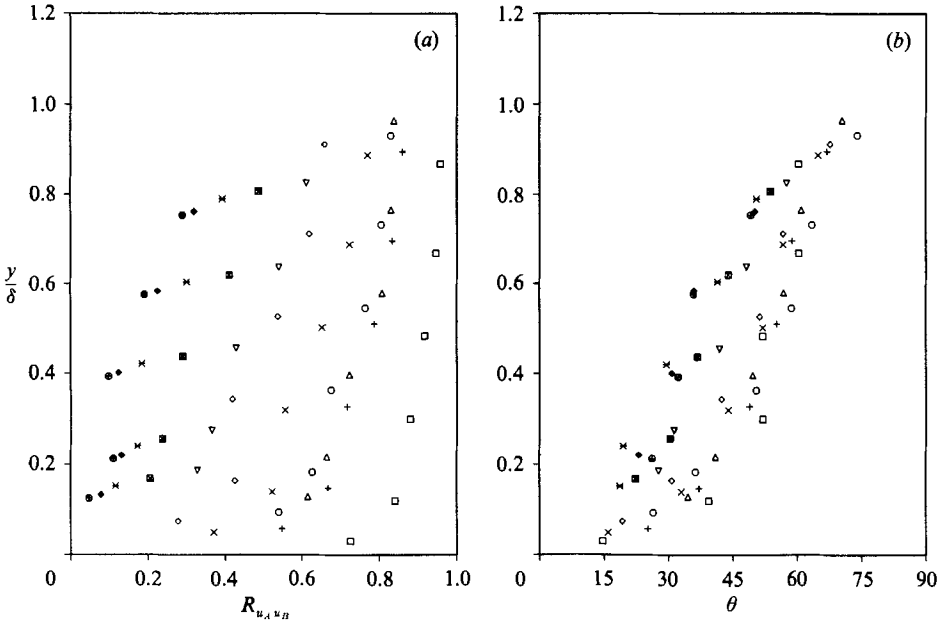

FIGURE 20. First recovery station ($s/\delta_0 = 3$). (*a*) Peak values of the cross-correlation; (*b*) average structure angle as a function of ξ/δ: □, $\xi/\delta = 0.016$; ○, 0.033; △, 0.035; +, 0.039; ×, 0.06; ◇, 0.07; ▽, 0.08; ⊠, 0.12; *, 0.15; ◇, 0.19, ⊕, 0.20.

However, for $\xi/\delta > 0.16$, the structure angle is independent of ξ within the scatter of the data. A possible explanation for this behaviour is the effect of the small-scale, more nearly isotropic eddies. For small ξ, small eddies can span both wires, and since they have a more random orientation, they tend to bias the cross-correlation towards $\tau = 0$ ($\theta = 90°$) on the average. As ξ increases, fewer isotropic eddies pass by both wires, and only the large-scale structures contribute to the cross-correlation. Thus, the results from the largest wire separations are probably more representative of the large-scale structure angle. This angle shows some variation across the layer; at $y/\delta = 0.3$, $\theta \sim 25°$–$35°$, while at $y/\delta = 0.8$, $\theta \sim 35°$–$45°$. For $y/\delta < 0.2$, the trend in θ and the results for smaller ξ imply that θ continues to decrease near the wall. This demonstrates the problem inherent in some previous approaches where the outer flow structure angle was measured with one sensor fixed at or near the wall (Brown & Thomas 1977; Robinson 1986). Such correlations will show an artificially large lag time (small angle) because of the small structure angle near the wall. Two travelling wires separated by a fixed distance give a measure of the *local* structure angle in the outer part of a boundary layer. The present results give quantitative experimental support to the conclusion Head & Bandyopadhyay (1981) drew from their smoke flow visualization: that a turbulent boundary layer consists largely of hairpin vortices inclined at 40°–50° to the wall, extending throughout the boundary layer. It is not clear that the correlations presented here are explicity due to hairpin vortices; however, they are consistent with the observation of large-scale structures spanning the entire shear layer.

For a given ξ, figure 19(*a*) shows that the peak in the cross-correlation is fairly constant across most of the boundary layer. This observation supports the idea that this technique detects the same structure at different points in the boundary layer; it also implies that similar structures fill the entire shear layer. However, the peak

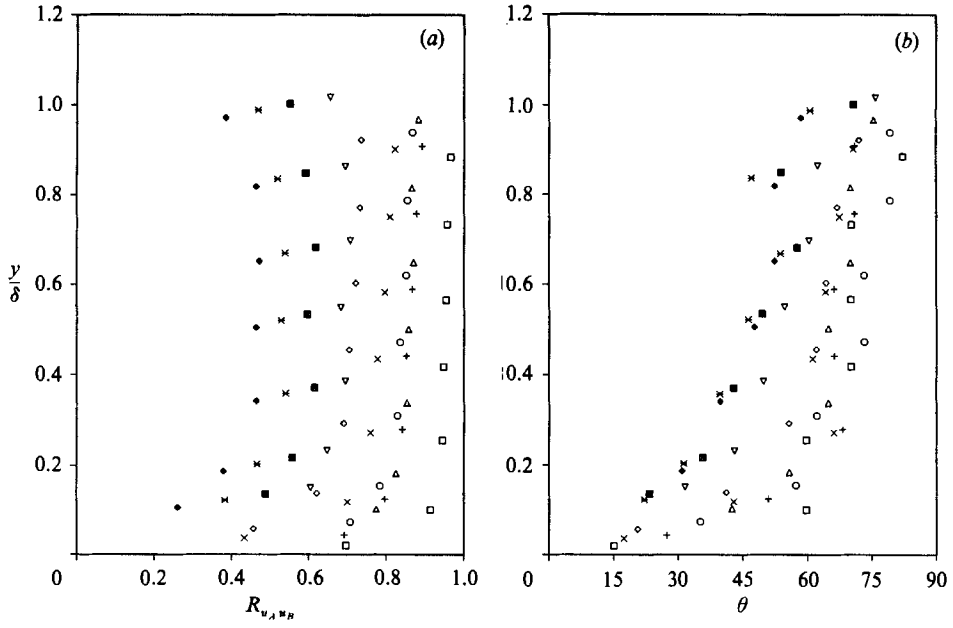

FIGURE 21. Station at $s/\delta_0 = 46$. (*a*) Peak values of the cross-correlation; (*b*) average structure angle as a function of ξ/δ: □, $\xi/\delta = 0.014$; ○, 0.028; △, 0.030; +, 0.033; ×, 0.047; ◇, 0.06; ▽, 0.07; ⊠, 0.10; *, 0.13, ◇, 0.16, ⊕, 0.25.

correlation falls off near the wall; the bars in figure 19(*a*) mark the wire locations for three sets of correlations for which one wire is at $y^+ = 30$ ($y/\delta = 0.02$). Clearly, the correlation in velocity fluctuations between the wall region and the outer flow is significantly less than the correlation between two points in the outer flow.

The peak cross-correlations and average structure angle are plotted in figures 20–22 for three streamwise locations after the end of curvature, at $s/\delta_0 = 3$, 46 and 91.

Near the exit from the bend, figure 20, the correlation levels are significantly lower than the upstream values for comparable ξ/δ, and this effect becomes more pronounced as y decreases for all wire separations shown. The increase in correlation with y may be a reflection of the suppressed turbulence intensities in the outer half of the boundary layer; however, even well into the outer layer the correlation level is lower than upstream.

In spite of the reduction in correlation level, the average structure angle at the end of curvature looks much the same as the upstream angle. Again, these angles measured for various ξ seem to converge for $\xi/\delta > 0.15$. Apparently, some large-scale structure does survive the curvature and it is still inclined to the wall at the upstream characteristic angle. This should not be taken to imply that the structure is unaffected by curvature. As indicated earlier, the boundary layer does not entrain new mass during the initial $\sim 12\delta_0$ of recovery, and the Reynolds stresses were strongly damped in the outer part of the layer during the initial recovery. Hence, the outer-layer 'structure' indicated in figure 16 cannot be very strong. The correlations are probably detecting the weakened remnants of the structure entering the bend, and this only because the background turbulence level is quite low.

Near the wall, the low correlation levels could indicate that the regrowing turbulence is extremely chaotic and that the concept of a 'typical' structure is

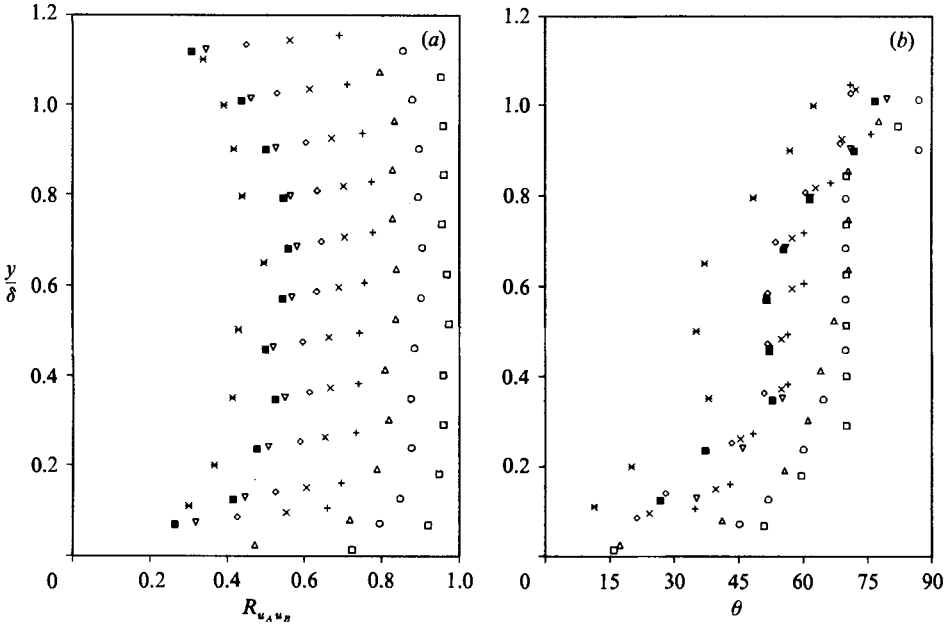

FIGURE 22. Last recovery station ($s/\delta_0 = 91$). (*a*) Peak values of the cross-correlation; (*b* average structure angle as a function of ξ/δ: □, $\xi/\delta = 0.010$; ○, 0.021; △, 0.033; +, 0.048; ×, 0.069; ◇, 0.088, ○, 0.11; ⊠, 0.12, *, 0.20.

inappropriate. Given the relatively large size of the stress bore after only $3\delta_0$ of recovery, it is clear that some extremely energetic mixing must occur following the step change in curvature. Thus the correlation levels could be washed out by the great variety in the individual coherent motions. Alternatively, the changes in the correlation levels could reflect a change in shape of the average structure. As pointed out by Perry, Li & Marusic (1988) and Fernando & Smits (1988) the mean velocity profile $U(y)$ depends only on the distribution of transverse vorticity, whereas all components of vorticity contribute to the Reynolds stresses. The reduction in mean shear caused by the step change *to* convex curvature may indicate that the vorticity of the large structures is realigned towards the streamwise direction. Realignment of the vorticity of the large-scale structures towards the streamwise direction would tend to increase $\overline{v^2}$ and $\overline{w^2}$ but both of these quantities are reduced in the outer region of the layer after curvature. Therefore if realignment of the vorticity has occurred the structures in the outer layer must be extremely weak. The reduced strength of the vorticity could be the result of cancellation of regions of vorticity of opposite sign caused by a more rapid merging of the 'legs' of the structures, as a result of the curvature. Similarly, after the step change back to the flat plate, the regrowth in the skin friction may signal another reorientation of the new structures formed at the wall. As these structures grow away from the wall into the structures created within or before the bend, the two-point correlation measurements could be washed out by the dissimilarity of the structures contributing to the correlation.

As the perturbed boundary layer relaxes on the flat plate, the cross-correlation for a given wire separation becomes constant with y, at levels comparable with the upstream levels of similar values of ξ/δ and, the average structure angle follows the same distribution as in the upstream unperturbed layer.

6. Concluding remarks

The state of the outer part of the boundary layer at the first recovery station indicates the effect of the curvature perturbation. Some large-scale structure does appear to survive the bend but it is greatly weakened and largely inactive. It cannot effectively transport momentum (low shear stress) and it does not entrain new fluid into the layer. Spectral measurements show a decrease in the low-frequency fluctuations. These results are consistent with the measurements and speculations of earlier workers.

In the recovery from the effects of curvature, the behaviour of the mean flow and the turbulence has been shown to be qualitatively quite different. In the first $10\delta_0$, the mean flow recovery is fast, and pressure gradient effects may be important in the results reported here. Subsequently the relaxation rate decreases and the mean flow parameters approach the flat plate levels asymptotically (and monotonically). One important aspect of these measurements is the documentation of the skin friction behaviour and its implication for drag reducation. The relaxation behaviour of the skin friction measurements from all available experiments were shown to scale on s/δ_0, once the effects of the pressure gradient history had dissipated. In the present experiment, the skin friction doubled in the first $10\delta_0$ of recovery, so that any drag reduction benefits from curvature appear to be relatively short-lived.

The turbulence relaxation process is much more complicated. The initial response to the step change in curvature (and to the pressure gradient over the first $8\delta_0$) is seen in the wall region, where the Reynolds stresses are regenerated. The stresses move outward via a stress bore, and turbulent transport is an important mechanism in this process. The stress ratios within the bore are very similar to those in the unperturbed profile, implying that the stress redistribution mechanism is unchanged in the relaxing boundary layer. The regrowth of the stress levels is accompanied by an increase in the low-frequency fluctuations. An analysis of the statistics of the fluctuations implies that the stress bore is similar to an inner boundary layer growing into a passive turbulent outer field, and presumably this inner field includes organized vortical structures typical of the new flat plate boundary condition.

Baskaran, Smits & Joubert (1987) suggested that internal layers are found in response to steps changes in curvature when $\Delta k^* > 0.37 \times 10^{-4}$, where $\Delta k^* = \nu/Ru_{\tau_0}$. In this flow, $\Delta k^* \approx 0.7 \times 10^{-4}$. However, the mean velocity and the Reynolds stress level in the inner part of the layer both change rapidly once the curvature is removed, which is more characteristic of the response to step changes in pressure gradient. Thus the initial recovery is partially driven by the short region of favourable pressure gradient for $s/\delta_0 < 8$. This could account for the different initial relaxation behaviour seen by Gillis & Johnston; in their study pressure gradient effects were an order of magnitude smaller, and the changes in Reynolds stresses were not accompanied by a regrowth in fullness of the mean velocity profile. Therefore, although the internal layer may be a useful concept, it seems too simplistic to describe accurately the details of the recovery behaviour observed in the present experiment. Given the extent of the stres bore at the first recovery station, it is clear that the virtual origin of this internal layer must be *upstream* of the step change in curvature.

It seems an oversimplification to state (Baskaran *et al.* 1987) that an internal layer developed in response to step changes in curvature grows completely independent of the outer layer. In the present case, it is difficult to see how the structures regrowing from the wall could be uninfluenced by the appreciable turbulence levels in the outer part of the layer, and it seems that the weak large-scale structures which are present

must at least affect the boundary conditions on the inner layer. In any case, the concept of an independent internal layer cannot be useful for a long distance downstream. In the present case, the stress bore fills the whole mean shear layer at a distance $20\delta_0$–$25\delta_0$ after the end of curvature, and yet the boundary layer is still very far from resembling a typical flat plate layer.

In addition, the stresses remain much larger than their self-preserving values even far downstream. As noted earlier, Gillis & Johnston, and Smits *et al.* (1979) also measured high stress levels at their farthest downstream stations ($s/\delta_0 \approx 40$ and 60, respectively). The stress levels remain high for the rest of the recovery, and it is only at the last two measuring stations that any reduction occurs, and then only slowly. The falling stress levels are accompanied by small changes in the stress ratios. These changes are rather subtle but they support the idea that some stable reorganization of the large-scale structure must be responsible for the longevity of the elevated stress levels. The relaxation rate eventually decreases to a point where the timescales are much longer than the large-eddy time scales. Even if we take the point where the mean velocity profiles have fully recovered ($\delta/\delta_0 = 46$) to mark the beginning of the final stress relaxation, then at a distance of more than 30 local boundary layer thicknesses downstream ($s/\delta_0 = 91$), little relaxation has actually occurred. If 10δ is a reasonable measure of the distance over which large eddies retain their identity, then these eddies are being replicated in some persistent, quasi-stable cycle.

Apart from its implications for the large-scale structure, the fact that the relaxation is not complete so far downstream after the end of curvature brings into doubt whether any boundary layer is every truly independent of its conditions of formation. This observation, in turn, casts further doubt on the concept of the standard 'universal' flat plate boundary layer.

This work was supported by AFOSR under Grants 85-0126 and 88-0120, monitored by Dr J. McMichael. The support of the National Science Foundation Graduate Fellowship Program and the Fannie and John Hertz Foundation is also gratefully acknowledged. Some of the data shown in figure 22 were obtained with the invaluable help of Mr R. W. Smith.

REFERENCES

Alving, A. E. 1988 Boundary layer relaxation from convex curvature. Ph.D. thesis, Princeton University.

Baskaran, V., Smits, A. J. & Joubert, P. N. 1987 A turbulent flow over a curved hill. Part 1. Growth of an internal layer. *J. Fluid Mech.* **182**, 47–82.

Bradshaw, P. 1973 The effect of streamline curvature on turbulent flow. *AGARDograph* 169.

Bradshaw, P., Ferriss, D. H. & Atwell, N. P. 1967 Calculation of boundary-layer development using the turbulent energy equation. *J. Fluid Mech.* **28**, 593–616.

deBrederode, V. & Bradshaw, P. 1974 A note on the empirical constants appearing in the logarithmic law for turbulent wall flows. *I. C. Aero. Rep.* 74–03. Aeronautics Dept., Imperial College, London.

Brown, G. L. & Thomas, A. S. W. 1977 Large-structure in a turbulent boundary layer. *Phys. Fluids* **20**, 243–252.

Bushnell, D. M. 1983 Turbulent drag reduction for external flows. *AIAA Paper* 83–0227.

Castro, I. P. & Bradshaw, P. 1976 The turbulence structure of a highly curved mixing layer. *J. Fluid Mech* **73**, 265–304.

Cheng, C. P. & Blackwelder, R. F. 1978 Large-scale motion in a turbulent boundary layer: a study using temperature contamination. *J. Fluid Mech.* **89**, 1–31.

Erm, L. P., Smits, A. J. & Joubert, P. N. 1987 Low Reynolds number turbulent boundary layers

on a smooth flat surface in a zero pressure gradient. *Fifth Symposium on Turbulent Shear Flows* (ed. F. Durst *et al.*). Springer.

FERNANDO, E M. & SMITS, A. J. 1988 Simple vortex loop model for turbulent boundary layers. *AIAA Paper* 88–3657.

GILLIS, J. C. & JOHNSTON, J. P. 1983 Turbulent boundary layer flow and structure on a convex wall and its redevelopment on a flat wall. *J. Fluid Mech.* **135**, 123–153.

GILLIS, J. C., JOHNSTON, J. P., MOFFAT, R. J. & KAYS, W. M. 1980 Turbulent boundary layer on a convex, curved surface. *Rep* HMT-31. Stanford University, Dept. of Mech. Engng.

HEAD, M. R. & BANDYOPADHYAY, P. 1981 New aspects of turbulent boundary layer structure. *J. Fluid Mech* **155**, 441–464.

KLEBANOFF, P. S. 1955 Characteristics of turbulence in a boundary layer with zero pressure gradient. *NACA Rep.* 1247.

LU, S. S. & WILLMARTH, W. W. 1973 Measurements of the structure of the Reynolds stress in a turbulent boundary layer. *J. Fluid Mech.* **60**, 481–511.

PATEL, V. C. 1965 Calibration of the Preston tube and limitations on its use in pressure gradients. *J. Fluid Mech.* **23**, 185–208.

PERRY, A. E. 1982 *Hot-Wire Anemometry*. Oxford University Press. 184 pp.

PERRY, A. E., LI, J. D. & MARUSIC, I. 1988 Novel methods of modeling wall turbulence. *AIAA Paper* 88–0219.

RAJAGOPALAN, S. & ANTONIA, R. A. 1979 Some properties of the large-structure in a fully developed turbulent duct flow. *Phys. Fluids* **22**, 614–622.

ROBINSON, S. K. 1986 Instantaneous velocity profile measurements in a turbulent boundary layer. *Chem. Engng. Commun.* **43**, 347–369.

SCHLICHTING, H. 1979 *Boundary Layer Theory* 7th ed. McGraw Hill.

SMITS, A. J., MATHESON, N. & JOUBERT, P. N. 1983 Low-Reynolds-number turbulent boundary layers in zero and favorable pressure gradients. *J. Ship Res.* **27**, 147–157.

SMITS, A. J., YOUNG, S. T. B. & BRADSHAW, P. 1979 The effect of short regions of high surface curvature on turbulent boundary layers. *J. Fluid Mech.* **94**, 209–242.

SO, R. M. C. & MELLOR, G. L. 1973 Experiment on convex curvature effects in turbulent boundary layers. *J. Fluid Mech.* **60**, 43–62.

SPINA, E. F. & SMITS, A. J. 1987 Organized structure in a compressible turbulent boundary layer. *J. Fluid Mech.* **182**, 85–109.

WATMUFF, J. H. 1979 Phase-averaged large-scale structures in three-dimensional turbulent wakes, Ph.D. thesis, University of Melbourne, Melbourne, Australia.

YOUSSEFMIR, P. 1982 Flow studies of full coverage film cooling on a convexly curved surface. Engng thesis, Stanford University, Stanford, CA.